Contributions to Mineralogy and Petrology (2022) 177:36
https://doi.org/10.1007/s00410-022-01892-y

ORIGINAL PAPER

In-situ Raman spectroscopic analysis of dissolved silica structures in Na_2CO_3 and NaOH solutions at high pressure and temperature

Naoko Takahashi[1] · Tatsuki Tsujimori[1,2] · Seiji Kamada[1,3,4] · Michihiko Nakamura[1]

Received: 3 September 2021 / Accepted: 18 January 2022 / Published online: 4 March 2022

Abstract

The dissolved silica structures in quartz-saturated 0.50 and 1.50 *m* [mol kg H_2O^{-1}] Na_2CO_3 and 0.47 *m* NaOH solutions at up to 750 °C and 1.5 GPa were investigated by in-situ Raman spectroscopy using a Bassett-type hydrothermal diamond anvil cell. The solubility of quartz in the solutions was determined by in-situ observations of the complete dissolution of the grain. The Raman spectra of the quartz-saturated Na_2CO_3 and NaOH solutions at high pressures and temperatures exhibited the tetrahedral symmetric stretching band of silica monomers. The lower frequency and broader width of the band than those in pure H_2O indicated the presence of both neutral and deprotonated monomers. In addition, we newly confirmed the intense bridging oxygen band and the tetrahedral symmetric stretching band of Q^1 (silicate center having a single bridging oxygen atom) in the spectra of the Na_2CO_3 solutions. The integrated intensity ratios of the bridging oxygen band to the monomer band increased with the addition of Na_2CO_3 and NaOH to fluids, corresponding to an elevation of the measured quartz solubilities. These observations indicate that the formation of silica oligomers in addition to neutral and deprotonated monomers explains the high dissolved silica concentrations in the solutions. The presence of deprotonated monomers under the experimental conditions suggests that deprotonated oligomers exist in the solutions, because the production of the latter more significantly reduces the Gibbs free energy. The anionic silica species and oligomers formed in alkaline silicate fluids may act as effective ligands for certain metal ions or complexes in deep subduction zones.

Keywords Hydrothermal diamond anvil cell · In-situ Raman spectroscopy · Quartz solubility · Silica speciation · Deprotonated monomer · Silica oligomer

Introduction

Aqueous fluids facilitate the mass transport of elements for the deep hydrothermal processes involved in metamorphism, metasomatism, and ore formation in the crust and upper mantle of the Earth. Silica is a major constituent of rock-forming minerals and is abundantly dissolved in the deep aqueous fluids. The mobilization of silica by the aqueous fluids has been observed as quartz veins and silica metasomatic zones of exhumed subduction zone rocks (Bebout and Barton 1989; Yardley and Bottrell 1992; Breeding and Ague 2002) and quartz-rich regions in the lower forearc crust with low Poisson's ratios (Audet and Bürgmann 2014; Hyndman et al. 2015). Understanding the efficiency of silica transportation in the deep crust and upper mantle requires detailed knowledge of silica solubility and speciation in aqueous fluids under high pressure (*P*) and temperature (*T*) conditions. Because of such importance, a significant number of experimental studies have been conducted on quartz solubility in pure H_2O (e.g., Anderson and Burnham 1965; Manning 1994), H_2O–CO_2 (e.g., Newton and Manning 2000; Shmulovich et al. 2001), and H_2O–NaCl fluids (e.g., Newton and Manning 2000; Shmulovich et al. 2006).

For SiO_2–H_2O systems, the solubility of quartz in pure H_2O increases with higher *P* and *T* (e.g., Anderson

Communicated by Hans Keppler.

✉ Naoko Takahashi
naoko.takahashi.t1@dc.tohoku.ac.jp;
n.takahashi.q46@gmail.com

[1] Department of Earth Science, Graduate School of Science, Tohoku University, Aoba, Sendai 980-8578, Japan

[2] Center for Northeast Asian Studies, Tohoku University, Aoba, Sendai 980-8576, Japan

[3] Frontier Research Institute for Interdisciplinary Sciences, Tohoku University, Aoba, Sendai 980-8578, Japan

[4] AD Science Inc., Funabashi, Chiba 273-0005, Japan

and Burnham 1965; Manning 1994), and this increase in the solubility is associated with the polymerization of aqueous silica monomers to form dimers or more polymerized species (e.g., Newton and Manning 2002, 2008; Zotov and Keppler 2002; Mysen 2010; Mysen et al. 2013). These experiments were conducted at near-neutral pH conditions, whereas the solubility behavior of quartz in high pH fluids could provide some insights into the nature of alkaline fluids in subducting lithologies such as crustal pelite (Galvez et al. 2015, 2016), crustal basalt (Galvez et al. 2016), and sediments (Connolly and Galvez 2018). The enhanced silica solubility in high pH fluids has been confirmed by early and recent studies on supercritical Na_2CO_3 or NaOH solutions (Friedman 1948; Anderson and Burnham 1967; Schmidt 2014; Aranovich et al. 2020). Aranovich et al. (2020) have systematically investigated quartz solubility in Na_2CO_3 and NaOH solutions at 500–700 °C and 0.4 and 0.5 GPa using an internally heated pressure vessel and a phase assemblage bracketing method. The results showed the quartz solubility systematically increased with greater salt concentrations, reaching 4.1 *m* [mol kg H_2O^{-1}] of silica in 3.5 *m* Na_2CO_3 and 2.4 *m* silica in 2.2 *m* NaOH. To describe the high solubility of quartz based on the equilibration between aqueous species, those authors considered the presence of deprotonated silica dimers [$Si_2O(OH)_5O^-$], in addition to the known silica monomeric and oligomeric species [$Si(OH)_4$, $Si(OH)_3O^-$, $Si_2O(OH)_6$, and $Si_3O_2(OH)_8$] in the solutions. Till date, there is a Raman spectroscopic study on quartz + 1.6 *m* Na_2CO_3 solution up to 600 °C and 1.5 GPa by Schmidt (2014). The Raman spectra revealed the presence of neutral monomers $Si(OH)_4$ and deprotonated monomers $Si(OH)_3O^-$ in the solutions, but lacked evidence of silica oligomers in the spectral region of interest (> ~ 700 cm^{-1} for the observation of carbon species). On the other hand, a Raman spectroscopy study with SiO_2–NaOH–H_2O systems by Mysen (2018) showed the Q^1-species band under high *P*–*T* conditions, but the presence of anionic silica species in the solution is still uncertain. Thus, the information available on the Raman observations is insufficient to understand silica solubility and speciation in Na_2CO_3 and NaOH solutions under high *P*–*T* conditions.

In the present study, we report the dissolved silica structures in quartz-saturated 0.50 and 1.50 *m* Na_2CO_3 and 0.47 *m* NaOH solutions up to 750 °C and 1.5 GPa by in-situ Raman spectroscopy in the silicate network vibration frequency range. In addition, we measured the solubility of quartz by in-situ observations of the complete dissolution of the quartz grain, which allowed for comparison with the Raman spectroscopy results. This information provides insights into silicate speciation and fluid–rock interactions for deep geological environments with the presence of alkaline hydrothermal fluids.

Experimental methods

Hydrothermal diamond anvil cell experiment

The experiments were performed using a Bassett-type hydrothermal diamond anvil cell (HDAC-V; Anderson et al. 2010). The cell utilized low-fluorescence-grade natural diamond anvils with a culet diameter of 800 µm. Gaskets with an initial thickness of 125 µm and an initial hole diameter of 400 µm, with pure water in the hole, were preheated to approximately 600–700 °C to avoid substantial deformation of the gasket at elevated *P*–*T*. An Ar + 2% H_2 mixture was introduced into the gas chamber during the experiments to prevent oxidation of the molybdenum heating wires and anvils at high *T*. The temperature was measured using K-type thermocouples, with each junction close to the upper and lower anvils. The temperature of the sample chamber was calibrated by direct observation of the melting of Sn (231.9 °C) and NaCl (800.7 °C), and the disappearance of the Raman 355 cm^{-1} band from the α-quartz at the α–β transition (574 °C) at ambient pressure. The pressure was calculated from the Raman frequency shift of the ~ 464 cm^{-1} quartz peak (Schmidt and Ziemann 2000) at *T* < 560 °C, and the ~ 1008 cm^{-1} zircon peak at *T* > 560 °C (Schmidt et al. 2013). The positions of the Raman peaks were normalized to the simultaneously obtained neon emission lines. The estimated pressure uncertainties of the reproducibility and random error for the quartz and zircon sensors are approximately 25 and 50 MPa, respectively (Schmidt and Ziemann 2000; Schmidt et al. 2013). For one experiment with a quartz-undersaturated system, the pressure was approximated from the isochore corresponding to the liquid–vapor homogenization temperature obtained during heating, based on the equation of state (EoS) of H_2O (Wagner and Pruβ 2002).

The present study included three series of experiments: (1) quartz + pure H_2O, (2) quartz + 0.50 and 1.50 *m* Na_2CO_3, and (3) quartz + 0.47 *m* NaOH. Sodium carbonate and sodium hydroxide (FUJIFILM Wako Pure Chemical Co. Japan) and deionized distilled water were used to prepare the solutions. The NaOH concentration was titrated with oxalic acid solution. Natural quartz (Minas Gerais, Brazil) and natural zircon (Mud Tank, Australia) were used as the starting crystals and the pressure sensors. After loading the quartz and zircon, the sample chamber was filled with the applicable solution and promptly sealed (within several seconds) to avoid concentration changes due to evaporation. It should be noted that the volume of air bubbles in the sample chamber was not controlled by the evaporation process under ambient conditions. We measured the volume of the quartz pieces to determine

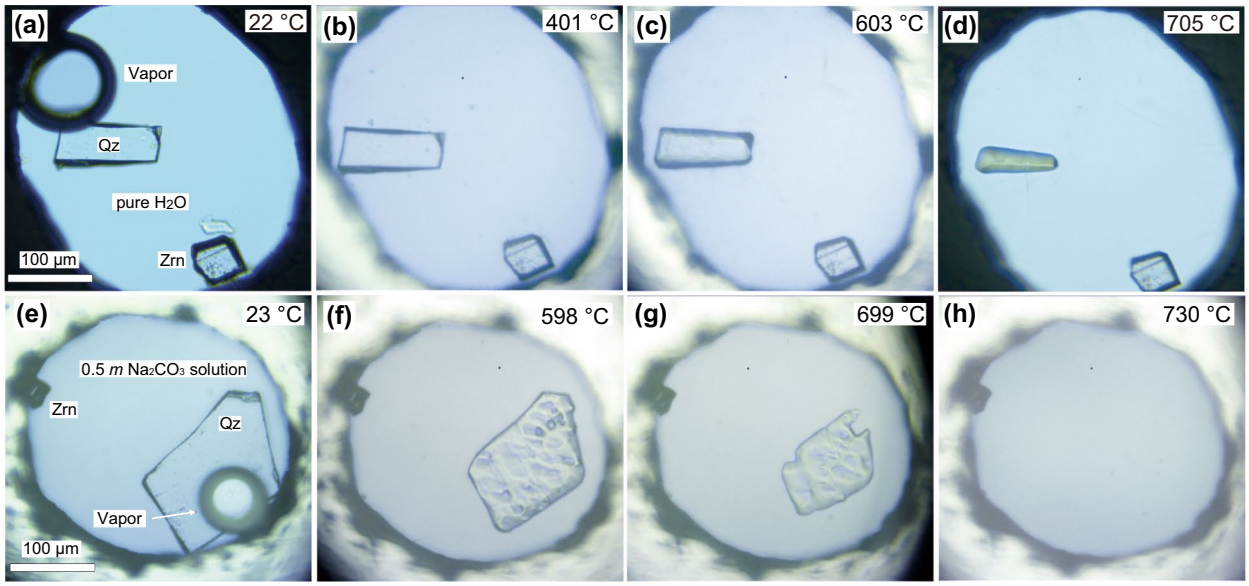

Fig. 1 **a** Photomicrograph of a sample chamber containing a piece of quartz and zircon and pure H_2O at 22 °C (QW4). **b**–**d** The views at 401 °C, 0.51 GPa, 603 °C, 0.70 GPa, and 705 °C, 0.89 GPa, respectively. The quartz became smaller with increasing *P* and *T*. The quartz was completely dissolved at 728 °C and 0.96 GPa in this experiment. **e** Photomicrograph of a sample chamber containing a piece of quartz and zircon and the 0.50 *m* Na_2CO_3 solution at 23 °C (QCF12). **f**, **g** The views at 598 °C, 0.97 GPa and 699 °C, 1.35 GPa, respectively. **h** The quartz dissolution was completed at 730 °C, 1.52 GPa

the solubility under the *P*–*T* conditions in which quartz was completely dissolved (Fig. 1). The surface areas of doubly polished sections of quartz were calculated based on the optical microscopic images. As the quartz pieces were not perfectly rectangular parallelepipeds, because the polished section of the quartz were manually broken, as shown in Fig. 1a, e, the surface areas were segmented into transparent parts and rim parts with weak transparency, using the Trainable Weka Segmentation (TWS) plugin of the Fiji ImageJ software (Schindelin et al. 2012; Arganda-Carreras et al. 2017). These processes allowed us to calculate the lower and upper limits of the surface areas of

Table 1 Experimental conditions and solubility results

Run#	Starting materials	*T* (°C)	*P* (GPa)	Measured Qz solubility (mol kg H_2O^{-1})[a]	Calculated Qz solubility in H_2O (mol kg H_2O^{-1})[b]
QW4	Qz, Zr, H_2O	728	0.96	0.72–0.95	0.72
QW5	Qz, Zr, H_2O	718	1.04	0.62–0.82	0.77
QCF13	Qz, Zr, 0.50 *m* Na_2CO_3	579	0.92	0.81 (13)–0.93 (15)	0.29
QCF15	Qz, Zr, 0.50 *m* Na_2CO_3	635	0.84	1.00 (12)–1.31 (15)	0.40
QCF20	Qz, Zr, 0.50 *m* Na_2CO_3	695	1.42	1.26 (41)–1.39 (45)	0.77
QCF12	Qz, Zr, 0.50 *m* Na_2CO_3	730	1.52	2.40 (31)–2.70 (35)	1.00
QCF18	Qz, Zr, 1.50 *m* Na_2CO_3	558	1.20	1.70 (11)–1.88 (12)	0.29
QCF19	Qz, Zr, 1.50 *m* Na_2CO_3	629	1.41	2.22 (52)–2.38 (56)	0.51
QCF11	Qz, Zr, 1.50 *m* Na_2CO_3	648	1.31	3.13 (35)–3.48 (38)	0.55
QSH3	Qz, Zr, 0.47 *m* NaOH	751	1.39	1.50 (38)–1.91 (48)	1.07

T, temperature; *P*, pressure; Qz, quartz; Zr, zircon

[a]Quartz solubility in H_2O and Na_2CO_3 and NaOH solutions determined by in-situ observations of quartz complete dissolution. Solubility ranges are based on the maximum and minimum volume of quartz crystal. Numbers in parentheses reflect the propagation of uncertainty from averaged two standard deviations of the solution density residual (see text)

[b]Quartz solubility in H_2O at *P* and *T* calculated based on the DEW model (Sverjensky et al. 2014; Huang and Sverjensky 2019)

the quartz piece, resulting in the solubility ranges shown in Table 1. To measure the quartz piece thickness, the other face of the fractured surface of each broken starting piece was imaged by tilting it at 20° or 25° in a field emission scanning electron microscope (FE-SEM; JEOL JSM-7001F). The fluid mass calculation was based on the method of Audétat and Keppler (2005), and the bubble volume was calculated using optical microscopic images obtained below liquid–vapor homogenization temperatures. The densities of the studied fluids at a given T and vapor-saturated P were calculated from the EoS of H_2O (Wagner and Pruβ 2002) or a model with empirical coefficients for complex aqueous solutions (Laliberté 2009). We considered that the density of the Na_2CO_3 and NaOH solution is within the model value plus or minus twice the average standard deviation of the solution density residual (experimental–calculated density; 0.73 and 1.50 kg m^{-3} for Na_2CO_3 and NaOH solution, respectively; Laliberté 2009). This creates uncertainty in the lower and upper limits of the solubility values (Table 1). For the experiments with Na_2CO_3 and NaOH solution, we considered the air bubble volume during the sample loading to attain liquid–vapor homogenization at a temperature that does not significantly exceed ~ 100 and ~ 120 °C, as per the data used in Laliberté (2009). The solubility of quartz determined in the present study is shown in units of molality m (moles of solute per kg of H_2O, not of aqueous salt solution).

The sample chamber was heated at 30–40 °C min^{-1}. The Raman spectra of the fluids were acquired at 50 or 100 °C increments after holding the sample at each temperature for a few minutes. Before the quartz dissolution was completed, the heating rate was reduced to ~ 15 °C min^{-1}. Previous time-dependent measurements indicated that quartz and H_2O in a sample chamber with a similar hole size attained equilibrium within a few minutes at 600 °C (Zotov and Keppler 2002).

Raman spectroscopy

Raman analyses were performed using a HORIBA Jobin Yvon LabRAM 300 Laser Raman microspectrometer connected to a 1024 × 256-pixel charge-coupled device (CCD) detector. Unpolarized Raman spectra of the fluids were recorded using a 632.82 nm He–Ne laser with default power and with a confocal hole of 500 µm, a slit width of 100 µm, 1800 lines mm^{-1} grating, and 2 or 3 accumulations of 240 s in the single spectral window (159.9–1194.8 cm^{-1}). The laser power measured at the sample surface with an Olympus SLMPLN 50 × objective lens (numerical aperture 0.35) was approximately 7 mW. The mechanical focus position was consistently at the culet surface of the upper diamond anvil. To compare the relative integrated intensities between the Raman spectra obtained under different P–T conditions, the spectra were corrected for the temperature factor of the Boltzmann distribution and the frequency and scattering factor (Brooker et al. 1988; Schmidt 2009). The spectra were further normalized by the density of the fluid and the factor for intensity decrease due to reflection at the diamond-fluid interface, according to the procedures described by Schmidt (2009) and Steele-MacInnis and Schmidt (2014). The density of supercritical H_2O fluids (Zhang and Duan 2005) was used for the supercritical Na_2CO_3 and NaOH solutions because of the lack of the EoS for the solutions at high P–T conditions. The corrected spectra were baseline-corrected using linear or polynomial functions and fitted by the Gaussian–Lorentzian area function using the software package PeakFit v4.12 (HULINKS Inc.).

Results

Solubility of quartz

Figure 1 shows the gradual dissolution of quartz in pure H_2O and 0.50 m [mol kg H_2O^{-1}] Na_2CO_3 solution along the experimental heating paths. A larger crystal was dissolved in the Na_2CO_3 solution than in pure H_2O at similar P–T values. The dissolution etch pits were characteristically observed on the crystal surface (Fig. 1f, g).

Table 1 and Fig. 2 summarize the results of quartz solubility in pure H_2O and Na_2CO_3 and NaOH solutions. In pure H_2O at 718 °C and 728 °C, and 1.0 GPa, the quartz solubilities fell in the range of 0.62–0.82 and 0.72–0.95 m, respectively. Although there was considerable uncertainty in the estimated quartz volume, the measured solubilities agreed, within the errors, with the values calculated based on the Deep Earth Water (DEW) model (0.72 and 0.77 m, respectively; Sverjensky et al. 2014; Huang and Sverjensky 2019) that used the solubility and speciation data for aqueous silica from high pressure experiments for characterizing the HKF coefficients. This agreement confirms the validity of the crystal-volume measurements in the present study.

The quartz solubilities determined for 0.50 and 1.50 m Na_2CO_3 solutions at 558–730 °C and 0.8–1.5 GPa were greater than those for pure H_2O at similar P–T conditions (Table 1). Even using the lowest estimation, the enhancing effect of the Na_2CO_3 on quartz solubility in aqueous fluids was confirmed. The quartz solubility increased at greater Na_2CO_3 concentrations, which is consistent with previous experimental data for up to approximately 4.7 m Na_2CO_3 solutions obtained at 300–450 °C and an unspecified P (Friedman 1948), and for 0.3–3.5 m Na_2CO_3 solutions obtained at 500–700 °C, and 0.4 and 0.5 GPa (Aranovich et al. 2020). The measured solubilities were generally similar to the values for 0.50 and 1.50 m Na_2CO_3 solution at 0.4 or

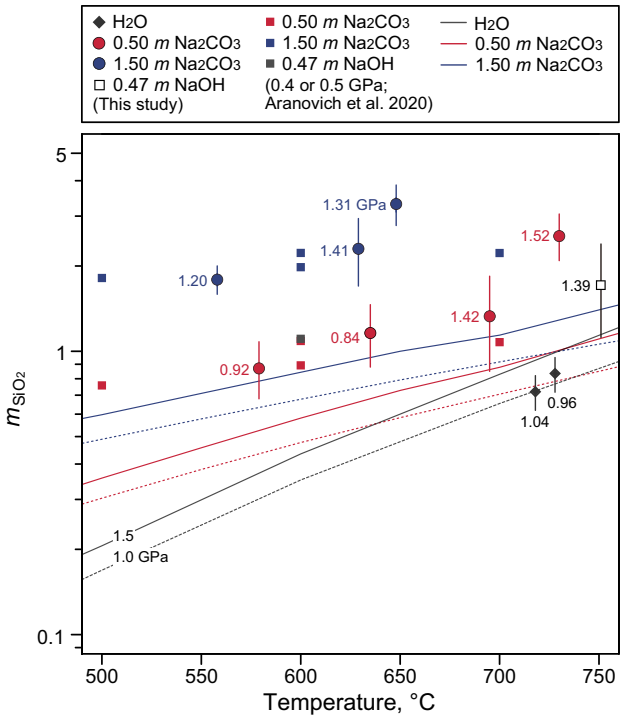

Fig. 2 Experimental results of quartz solubility in pure H_2O (black diamond), 0.50 *m* Na_2CO_3 (red circle), 1.50 *m* Na_2CO_3 (blue circle), and 0.47 *m* NaOH (black square) as a function of temperature. Each symbol represents the average of the upper and lower limits solubility, with the error bars including the uncertainties from the volume of the quartz crystal and the density of the solution. The values accompanying each symbol correspond to the pressure at which the quartz was completely dissolved. Filled square symbols are quartz solubility values in 0.50 and 1.50 *m* Na_2CO_3 and 0.47 *m* NaOH at 0.4 or 0.5 GPa, which are linearly interpolated or extrapolated from the data of Aranovich et al. (2020). Quartz solubilities in H_2O, 0.5 *m* Na_2CO_3, and 1.5 *m* Na_2CO_3 at 1.0 and 1.5 GPa calculated based on the DEW model (Sverjensky et al. 2014; Huang and Sverjensky 2019) and the EQ3NR code (Wolery 1992) are shown as dashed and solid lines for comparison

0.5 GPa calculated by linear interpolation of the Aranovich et al.'s (2020) data, except for the slightly higher results at 648 °C (1.3 GPa) and 730 °C (1.5 GPa) (Fig. 2). The quartz solubility in 0.47 *m* NaOH solution at 751 °C and 1.4 GPa overlapped within the errors with the value for 0.47 *m* NaOH solution at 0.4 GPa calculated by linear extrapolation of the Aranovich et al.'s (2020) data (Fig. 2).

Raman spectra and band assignments

Table 2 summarizes the results of Raman spectroscopic measurements. Figure 3 shows the unprocessed Raman spectra of the quartz-saturated and -undersaturated 1.50 *m* Na_2CO_3 solutions, and Fig. 4 presents those of the quartz-saturated 0.50 *m* Na_2CO_3 and 0.47 *m* NaOH solutions. The spectra, corrected for the frequency and temperature factors (Brooker et al. 1988; Schmidt 2009), were baseline-corrected by polynomial functions using the ~ 450–500 cm^{-1}, ~ 730 cm^{-1}, and ~ 900 or ~ 950 cm^{-1} regions as anchors. We did not include the higher frequency regions, in which the intensity increased due to the strong fluorescence of the diamond. In the spectra of the Na_2CO_3 solution, a simple linear baseline correction was applied to remove the background in the range of ~ 950–1150 cm^{-1} to obtain the relative intensities of the vibrational modes of the carbon species. Figure 5 shows the representative baseline-corrected Raman spectra fitted by the Gaussian–Lorentzian area function and the assignment of the vibrations of silicate species. In the following sections, we use the Q^n terminology, which represents the tetrahedral silicate center connected to *n* bridging oxygen atoms.

The ~ 600 cm^{-1} band region

In the ~ 500–700 cm^{-1} region, we observed an intense broad band in the Raman spectra of quartz-saturated 0.50 and 1.50 *m* Na_2CO_3 solutions (Figs. 3a and 4a), as well as in the quartz-undersaturated 1.50 *m* Na_2CO_3 solution (Fig. 3b). The observation of this band in the NaOH solution (Fig. 4b) was consistent with that reported by Mysen (2018). The band was detected above ~ 300–400 °C in the Na_2CO_3 solution, ~ 500 °C in the NaOH solution, and ~ 600 °C in pure H_2O. The band showed increased intensities and broadening to a lower frequency of ~ 500 cm^{-1} with increasing *P* and *T*. In some spectra, the band could be separated into at least two components, with a main band at ~ 600 cm^{-1} and a weaker band at ~ 650 cm^{-1} in the Na_2CO_3 solution (Fig. 5). Experimental and ab initio molecular dynamics studies have shown that the band near 600 cm^{-1} represents the vibrations of bridging oxygen Si–O–Si of weakly polymerized silica species such as dimers and trimers (e.g., Lasaga and Gibbs 1988; Zotov and Keppler 2000; Hunt et al. 2011; Spiekermann et al. 2012a, b). Spiekermann et al. (2012a) showed that the bridging oxygen symmetric stretching appeared as a major band at ~ 620 cm^{-1} and a shoulder band at ~ 680 cm^{-1} for dimers, and a major band at ~ 680 cm^{-1} for linear trimers. The ring trimer displays a band at ~ 500–600 cm^{-1} from the ring breathing mode, in addition to the prominent bridging oxygen band at ~ 600 cm^{-1} (Dutta and Shieh 1985; Hunt et al. 2011; Spiekermann et al. 2012b). These frequency ranges can cover the observed band in the 500–700 cm^{-1} region, which is interpreted as resulting from a dimer ± trimer formation. However, it may be challenging to assign the separated bands to individual oligomeric species, as the Si–O–Si vibrational frequencies may show a significant variability owing to the structural degree of freedom of the Si–O–Si bending angle (Kubicki and Sykes 1993; Hunt et al. 2011).

Table 2 Raman spectroscopy measurement conditions and results

Run#	Solution composition	T_h (°C)	T (°C)	P (GPa)	Phase	ω_{770} (cm^{-1})[a]	$FWHM_{770}$ (cm^{-1})[b]	A_{600}/A_{770}[c]	A_{1000}/A_{1060}[d]
QW6	H_2O	179.6	650	1.45	Qz + F	776.0 (0.2)	20.2 (0.7)	0.11 (3)	–[g]
			702	1.63	Qz + F	776.3 (0.2)	22.6 (0.8)	0.15 (3)	–
QW10	H_2O	184.9	603	0.76	Qz + F	773.5 (0.2)	18.1 (0.9)	0.13 (4)	–
			651	0.88	Qz + F	773.2 (0.2)	18.9 (0.9)	0.13 (4)	–
			702	1.02	Qz + F	772.9 (0.2)	20.4 (0.7)	0.11 (2)	–
			753	1.25	Qz + F	772.6 (0.3)	21.6 (0.8)	0.17 (5)	–
			801	1.47	Qz + F	772.7 (0.3)	21.9 (0.8)	0.26 (4)	–
QW12	H_2O	49.9	300	0.59	Qz + F	778.1 (1.2)	18.4 (4.8)	–	–
			400	0.83	Qz + F	777.5 (0.8)	18.0 (3.1)	–	–
			500	1.00	Qz + F	776.6 (0.5)	19.4 (1.9)	–	–
			592	1.11	Qz + F	776.0 (0.4)	19.7 (1.3)	0.27 (7)	–
QCF13	0.50 *m* Na_2CO_3	73.9	401	0.64	Qz + F	768.3 (1.0)	29.2 (2.7)	n.d.[h]	n.d.
			499	0.89	Qz + F	769.3 (0.7)	34.2 (2.2)	0.44 (9)	–
			579[e]	0.92[e]	F	769.6 (0.5)	31.2 (1.4)	0.42 (8)	–
QCF15	0.50 *m* Na_2CO_3	83.6	400	0.67	Qz + F	768.4 (0.9)	30.9 (2.5)	n.d.	n.d.
			499	0.59	Qz + F	765.6 (0.8)	33.0 (2.1)	n.d.	n.d.
			600	0.89	Qz + F	767.2 (0.5)	30.8 (1.5)	0.46 (9)	–
			635[e]	0.84[e]	F	767.6 (0.4)	31.4 (1.2)	0.40 (6)	–
QCF20	0.50 *m* Na_2CO_3	35.9	200	0.46	Qz + F	–	–	–	0.19 (4)
			300	0.72	Qz + F	772.6 (0.7)	26.0 (2.5)	0.41 (13)	0.65 (9)
			400	0.96	Qz + F	774.4 (0.3)	28.2 (1.1)	0.38 (9)	1.14 (12)
			500	1.32	Qz + F	774.4 (0.3)	28.3 (1.1)	0.45 (10)	1.43 (21)
			600	1.11	Qz + F	772.6 (0.3)	29.1 (1.0)	0.43 (4)	–
			695[e]	1.42[e]	F	773.7 (0.3)	28.5 (0.9)	0.52 (6)	–
QCF12	0.50 *m* Na_2CO_3	103.0	300	0.53	Qz + F	768.3 (1.4)	31.1 (4.5)	n.d.	n.d.
			400	0.76	Qz + F	769.7 (0.8)	29.4 (2.6)	0.56 (14)	n.d.
			500	0.96	Qz + F	770.3 (0.5)	30.9 (1.7)	0.58 (9)	n.d.
			598	0.97	Qz + F	771.5 (0.5)	29.7 (1.3)	0.52 (9)	–
			649	1.15	Qz + F	771.8 (0.4)	27.7 (1.2)	0.59 (7)	–
			699	1.35	Qz + F	772.9 (0.3)	27.8 (1.0)	0.49 (5)	–
			730[e]	1.52[e]	F	773.5 (0.3)	28.1 (0.9)	0.54 (6)	–
QCF18	1.50 *m* Na_2CO_3	83.3	200	0.38	Qz + F	–	–	–	0.16 (3)
			300	0.62	Qz + F	771.5 (0.8)	25.3 (2.7)	n.d.	0.45 (5)
			400	0.87	Qz + F	771.0 (0.5)	27.6 (1.2)	0.69 (14)	0.62 (5)
			500	1.07	Qz + F	770.9 (0.4)	29.4 (1.2)	0.76 (10)	0.85 (6)
			558[e]	1.2[e]	F	772.1 (0.3)	29.4 (0.9)	0.80 (8)	0.90 (6)
QCF19	1.50 *m* Na_2CO_3	41.3	100	0.25	Qz + F	–	–	–	0.07 (11)
			200	0.54	Qz + F	–	–	–	0.09 (2)
			300	0.81	Qz + F	774.1 (0.6)	23.3 (2.1)	0.53 (14)	0.31 (5)
			400	1.08	Qz + F	773.5 (0.4)	27.0 (1.2)	0.72 (12)	0.61 (4)
			500	1.32	Qz + F	773.1 (0.4)	28.3 (1.0)	0.71 (13)	0.87 (5)
			600	1.48	Qz + F	771.8 (0.3)	29.9 (0.8)	1.04 (9)	0.79 (5)
			629[e]	1.41[e]	F	771.9 (0.4)	29.8 (0.9)	1.00 (12)	0.71 (5)
QCF11	1.50 *m* Na_2CO_3	65.4	200	0.43	Qz + F	–	–	–	0.23 (3)
			300	0.67	Qz + F	–	–	–	0.67 (9)
			400	0.85	Qz + F	771.1 (0.4)	25.7 (1.6)	n.d.	0.61 (5)
			498	1.02	Qz + F	771.1 (0.5)	28.6 (1.5)	0.75 (12)	0.79 (9)
			600	1.25	Qz + F	771.3 (0.4)	31.3 (1.1)	0.95 (15)	0.81 (14)
			648[e]	1.31[e]	F	771.3 (0.4)	29.7 (1.1)	1.05 (11)	0.73 (8)

Table 2 (continued)

Run#	Solution composition	T_h (°C)	T (°C)	P (GPa)	Phase	ω_{770} (cm^{-1})[a]	$FWHM_{770}$ (cm^{-1})[b]	A_{600}/A_{770}[c]	A_{1000}/A_{1060}[d]
QCF21	1.50 *m* Na_2CO_3	30.7	200[f]	0.28[f]	F	n.d.	n.d.	n.d.	0.14 (2)
			300[f]	0.50[f]	F	n.d.	n.d.	n.d.	0.20 (3)
			400[f]	0.72[f]	F	771.2 (1.8)	26.8 (5.3)	1.39 (53)	0.18 (4)
			500[f]	0.93[f]	F	771.0 (1.3)	33.6 (4.8)	1.63 (29)	0.30 (2)
			603[f]	1.14[f]	F	767.9 (1.4)	34.6 (5.0)	1.51 (31)	0.29 (3)
			705[f]	1.35[f]	F	766.0 (1.1)	28.3 (3.9)	1.69 (27)	0.46 (3)
QSH3	0.47 *m* NaOH	115.0	300	0.51	Qz + F	768.6 (0.7)	25.3 (2.5)	n.d.	–
			400	0.72	Qz + F	768.6 (0.5)	28.6 (1.6)	n.d.	–
			500	0.88	Qz + F	770.2 (0.6)	30.3 (2.0)	n.d.	–
			599	1.00	Qz + F	770.2 (0.5)	29.4 (1.2)	0.27 (5)	–
			650	1.12	Qz + F	771.1 (0.4)	29.2 (1.2)	0.27 (4)	–
			701	1.27	Qz + F	771.9 (0.3)	27.6 (0.9)	0.32 (4)	–
			751[e]	1.39[e]	F	772.6 (0.3)	26.4 (0.9)	0.36 (4)	–

T, temperature; *P*, pressure; T_h, liquid–vapor homogenization temperature; Qz, quartz; F, fluid; V, vapor

[a]Frequency of the 770 cm^{-1} band assigned to the tetrahedral symmetric stretch of silica monomers. Numbers in parentheses represent two standard deviations

[b]Full width half at maximum (FWHM) of the 770 cm^{-1} band. Numbers in parentheses represent two standard deviations

[c,d]Ratio of the integrated intensities. Numbers in parentheses represent the uncertainty from the propagation of two standard deviation

[e]Qz dissolution was completed at this *P* and *T*

[f]Qz was undersaturated at this *P* and *T*

[g]The signals of the band were not observed

[h]n.d. represents that the integrated intensities or their ratios were not determined due to the poor signal to noise ratios

The ~ 770 cm^{-1} band region

The Raman spectra of quartz-saturated 0.50 and 1.50 *m* Na_2CO_3 and 0.47 *m* NaOH solutions showed prominent bands at ~ 770 cm^{-1} (Figs. 3a and 4). The intensities of the band increased with increasing *P*–*T* conditions in the quartz-saturated systems and were greater than those observed with pure H_2O (Fig. 5). This band can be readily assigned to the tetrahedral symmetric Si–O stretching of monomeric silica species (Lasaga and Gibbs 1988; Zotov and Keppler 2000; Spiekermann et al. 2012a, b). Figure 6 shows the frequency and full width at half maximum (FWHM) of the band in the quartz-saturated H_2O, Na_2CO_3, and NaOH solutions as a function of *T* (and *P*). The frequency in the Na_2CO_3 and NaOH solutions was lower than that in H_2O at similar *P*–*T* conditions (Fig. 6a). The FWHM of the band in H_2O increased with increasing *P* and *T* up to ~ 23 cm^{-1}. In contrast, the FWHM in the Na_2CO_3 and NaOH solutions exhibited greater values than ~ 25 cm^{-1} with all experimental conditions (Fig. 6b). The overall trends were similar for the Na_2CO_3 and NaOH solutions. Hunt et al. (2011) showed that the frequency of the tetrahedral symmetric stretching of deprotonated monomers [$Si(OH)_3O^-$] and doubly deprotonated monomers [$Si(OH)_2O_2^{2-}$] shifted to the lower frequency regions. The second deprotonation requires extremely high pH (> 13) under ambient conditions (Bergna and Roberts 2005); therefore, the observed low frequency and broad FWHM features of the band can be an indication of deprotonated monomers in addition to the presence of neutral monomers [$Si(OH)_4$]. Schmidt (2014) similarly assigned the two separated peaks of the broad band at ~ 770 cm^{-1} to the tetrahedral symmetric stretching of neutral and deprotonated monomers for quartz + 1.6 *m* Na_2CO_3 experiments up to 600 °C and 1.5 GPa. The present study indicated the prevalence of the deprotonated species in 0.50 and 1.50 *m* Na_2CO_3 and 0.47 *m* NaOH solutions equilibrated with quartz up to 750 °C and 1.5 GPa.

The ~ 800–900 cm^{-1} band regions

The Raman spectra of quartz-saturated 0.50 and 1.50 *m* Na_2CO_3 and 0.47 *m* NaOH solutions showed very weak band centered at ~ 830 cm^{-1} as a shoulder of the 770 cm^{-1} band (Figs. 3a and 4). This band can be attributed to the tetrahedral Si–O symmetric stretching of Q^1 units, i.e., dimeric silicates or chain silicate species, and the asymmetric stretching of the ethane-like dimer $Si_2O(OH)_6$, which appeared at 793 cm^{-1} and 783 cm^{-1}, respectively (Spiekermann et al. 2012a). The previous work by Schmidt (2014)

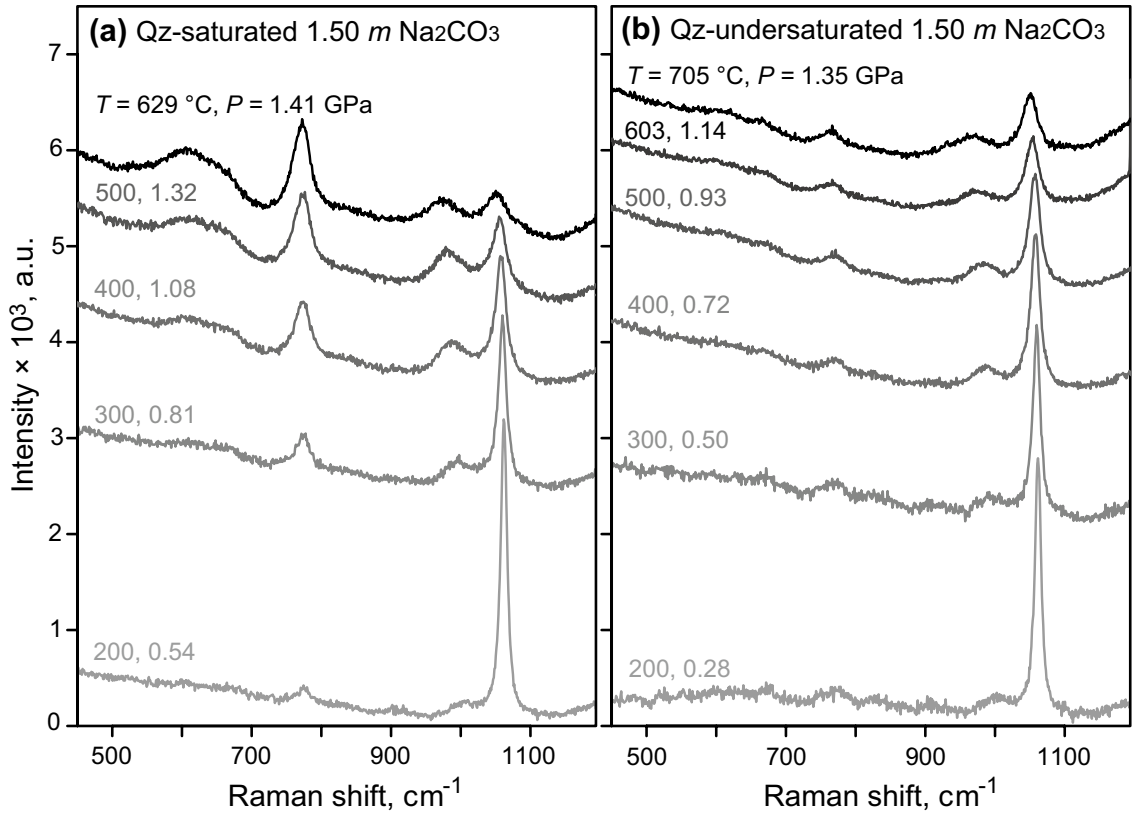

Fig. 3 Unprocessed Raman spectra of **a** quartz-saturated and **b** quartz-undersaturated 1.50 *m* Na_2CO_3 solutions at high *P*–*T* conditions

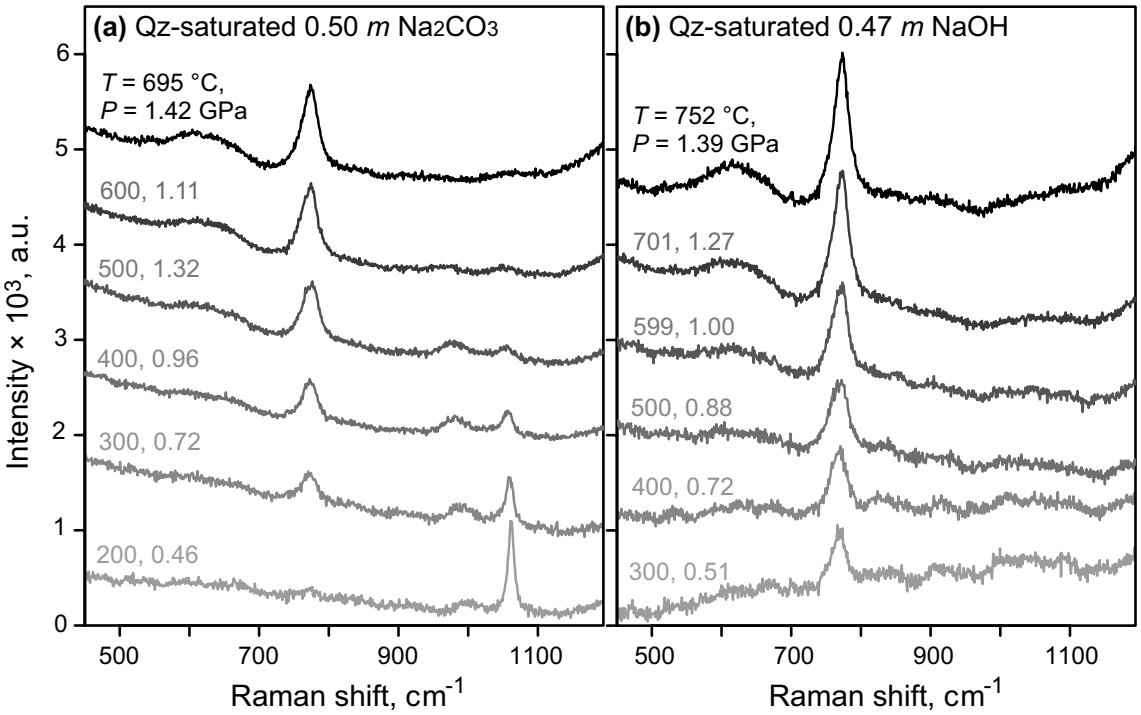

Fig. 4 Unprocessed Raman spectra of quartz-saturated **a** 0.50 *m* Na_2CO_3 solution and **b** 0.47 *m* NaOH solution at high *P*–*T* conditions

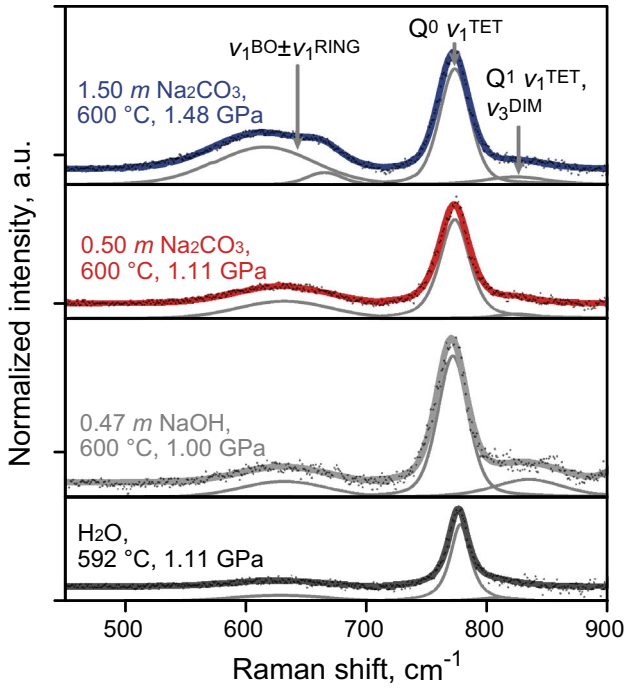

Fig. 5 The normalized and baseline-corrected Raman spectra data of the quartz-saturated H_2O, 0.47 *m* NaOH solution, 0.50 *m* Na_2CO_3 solution, and 1.50 *m* Na_2CO_3 solution (dots) with the components fitted by the Gaussian–Lorentzian area function (gray lines), and band assignments. The abbreviations of the vibrational mode of silica species are based on Spiekermann et al. (2012a, b): ν_1^{BO} = bridging oxygen symmetric stretch; ν_1^{RING} = symmetric breathing of ring trimer; ν_1^{TET} = tetrahedral symmetric stretch; ν_3^{DIM} = asymmetric stretch of the ethane-like dimer. See text for additional discussion of the band assignments

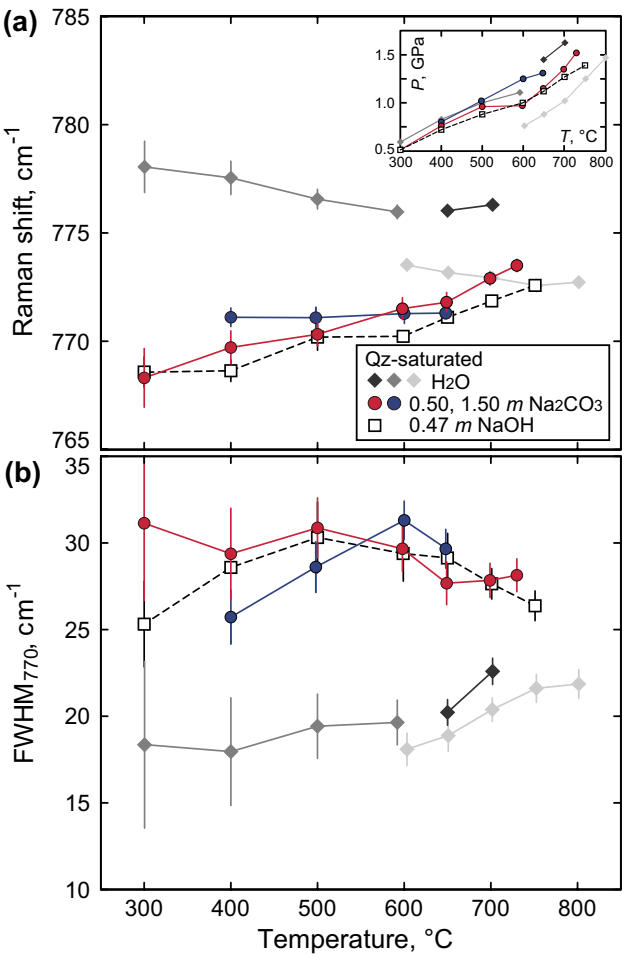

Fig. 6 **a** Frequency and **b** full width at half maximum (FWHM) of the 770 cm^{-1} bands as a function of temperature (and pressure), with two standard error bars. Inset of **a** represents the measurement *P*–*T* conditions

did not separate the band at ~ 830 cm^{-1}, possibly because of its low intensity.

In the Raman spectra of the quartz-saturated NaOH solution, the ~ 830 cm^{-1} band showed broadening to the frequency at ~ 950 cm^{-1} (Fig. 4b). The band at ~ 900 cm^{-1} was observed in the SiO_2–H_2O system (Zotov and Keppler 2002), but hardly detected in the 0.50 and 1.50 *m* Na_2CO_3 solutions, possibly because it overlapped with the stretching band of carbon species in the 1.50 *m* Na_2CO_3 solution. The ~ 900 cm^{-1} band has been assigned to Q^2 units, i.e., the cyclic silicate or middle group in silicate chains, in several studies, but using only this explanation could cause overestimation of the degree of polymerization, because there are several potential species that could be responsible for this band. Spiekermann et al. (2012a) showed that the tetrahedral symmetric stretching of Q^2 appears at 888 cm^{-1}, coupled with 1081 cm^{-1}. The presence of the broad band at ~ 950–1050 cm^{-1} in the NaOH solution is not likely to result only from the coupled features of Q^2, because the bridging oxygen Si–O–Si asymmetric stretching of Q^n or the Si–O^- stretching of the deprotonated species appears in these regions, as described below. The ~ 900 cm^{-1} band may include a contribution from the symmetric stretching of the ethane-like dimer $Si_2O(OH)_6$, which shows a band at 870 cm^{-1} (Spiekermann et al. 2012a). In addition, the tetrahedral asymmetric stretching of Q^0 and Q^1 and the single non-bridging Si–OH stretching of various Q^n units (n = 0–3) appear between 915 cm^{-1} and 936 cm^{-1} (Spiekermann et al. 2012a).

The ~ 1000 cm^{-1} band region

The Raman spectra of the quartz-saturated and -undersaturated 1.50 *m* Na_2CO_3 solutions showed prominent bands at ~ 1000 cm^{-1} and ~ 1060 cm^{-1} (Fig. 3). The ~ 1060 cm^{-1} bands in the quartz-saturated solution exhibited broader features than those of the quartz-undersaturated solution. These bands diminished to ~ 600–700 °C in the quartz-saturated 0.50 *m* Na_2CO_3 solution (Fig. 4a). These bands can be

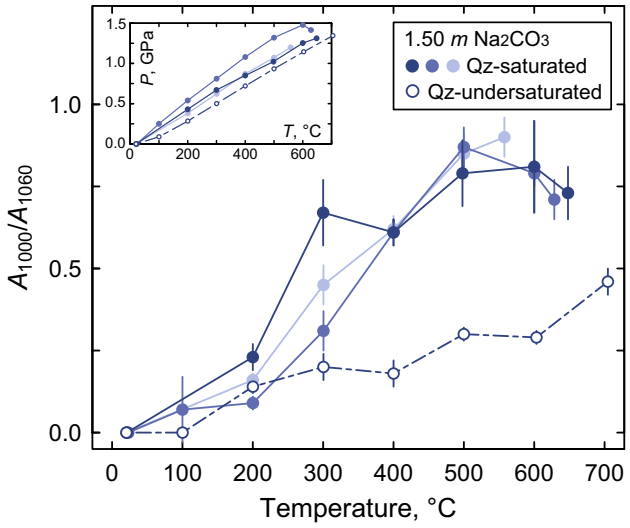

Fig. 7 The integrated intensity ratios of the ~1000 cm^{-1} band to the ~1060 cm^{-1} band as a function of temperature (and pressure) in the quartz-saturated and -undersaturated systems. The bands are mainly contributed from the C–OH stretching of HCO_3^- and the C–O symmetric stretching of CO_3^{2-}, respectively

mainly assigned to the C–OH stretching of HCO_3^- and the C–O symmetric stretching of CO_3^{2-}, respectively (Frantz 1998; Rudolph et al. 2008; Schmidt 2014). Figure 7 shows that the relative intensities of the ~1000 cm^{-1} band to the ~1060 cm^{-1} band (A_{1000}/A_{1060}) were higher in the quartz-saturated system than in the undersaturated system. At ~600 °C, the relative intensities in the quartz-saturated system remained constant or decreased. This is likely attributed to an intensity increase at ~1060 cm^{-1} owing to the contributions from the silicate species vibrations, as described below.

Broad, weak signals were detected in the high-frequency regions at ~950–1150 cm^{-1} in the quartz-saturated NaOH solution spectra (Fig. 4b). The ~1060 cm^{-1} region of the quartz-saturated 1.50 *m* Na_2CO_3 solution spectra also indicated the contribution from silicate species. The bands are likely attributed to the bridging oxygen Si–O–Si asymmetric stretching of Q^n ($n = 1$–4) at ~1070 cm^{-1} (Spiekermann et al. 2012a), because of the presence of the bridging oxygen vibrations at ~600 cm^{-1}. In addition, Spiekermann et al. (2012a) showed that the tetrahedral symmetric stretching of Q^2 and Q^3 units displays bands at 1081 cm^{-1} and 1103 cm^{-1}, respectively. Moreover, the tetrahedral asymmetric stretching of Q^2, Q^3, and Q^4 units exhibits bands centered at 970, 1015, and 1062 cm^{-1}, respectively. However, we may exclude contributions from the vibrations of Q^4 units, because those species were not detected in aqueous solutions of up to 40 mol% SiO_2 concentrations in $Na_2O{\cdot}2SiO_2$ (NS2)–H_2O and $Na_2O{\cdot}3SiO_2$ (NS3)–H_2O systems at high *P*–*T* conditions (Steele-MacInnis and Schmidt 2014). Another possibility is a contribution from the Si–O^- stretching of the deprotonated species centered at ~1050 cm^{-1} (Hunt et al. 2011). Although the high-frequency bands were not as prominent as those observed in highly alkaline silicate solutions at ambient *T* and up to 2.0 GPa (Dutta and Shieh 1985; Gout et al. 2000; Hunt et al. 2011), the bands may include contributions from the deprotonated species, because of the presence of the deprotonated monomer $Si(OH)_3O^-$.

Discussion

Comparisons with previous solubility data in Na_2CO_3 solutions

Aranovich et al. (2020) determined the quartz solubility in 0.2–3.5 *m* Na_2CO_3 solutions at conditions of 500, 600, and 700 °C and 0.4 GPa, and 600 °C and 0.5 GPa, using an internally heated pressure vessel and a phase assemblage bracketing method. Those authors showed a slight increase of quartz solubility in the Na_2CO_3 solutions with increasing *P* and *T*. Figure 2 shows that our measured solubilities in 0.50 *m* Na_2CO_3 solutions at 579 °C (0.92 GPa), 635 °C (0.84 GPa), and 695 °C (1.42 GPa), and 1.50 *m* Na_2CO_3 solutions at 558 °C (1.20 GPa) and 629 °C (1.41 GPa) overlapped, within errors, with the calculated values from the Aranovich et al. (2020) experiments at 0.4 and 0.5 GPa. This agreement indicates that the pressure dependence of the quartz solubility is negligible at these temperature and compositional ranges. In contrast, our measured solubilities in the 0.50 *m* Na_2CO_3 solution at 730 °C (1.52 GPa) and the 1.50 *m* Na_2CO_3 solution at 648 °C (1.31 GPa) were higher than the values extrapolated from the lower temperature results. This might suggest that the solubility of quartz becomes more dependent on temperature at higher *P* as *P*–*T* conditions approach the critical curve.

Schmidt (2014) reported the silica solubility in 1.6 *m* Na_2CO_3 solution at 600 °C and 1.5 GPa based on the in-situ Raman spectroscopic study to be ~1 *m*, which is approximately two times lower than our lowest estimation of the solubility in 1.50 *m* Na_2CO_3 at 629 °C and 1.41 GPa (2.22 ± 0.52 *m*). This discrepancy likely relates to the calculation used by Schmidt (2014) being based on the integrated intensities of the monomeric silica band. In the present study, the in-situ Raman spectroscopy in the frequency regions of silicate newly revealed the strong bridging oxygen band and the tetrahedral symmetric stretching band of the Q^1 unit in the quartz-saturated 1.50 *m* Na_2CO_3 solution spectra (Figs. 3 and 5), indicating the presence of silica oligomers in the solution. Therefore, basing the total silica solubility calculation solely on the integrated intensities of the monomeric silica band could lead to underestimation in this system. The present study shows the effect of the alkaline

Na_2CO_3 solution on enhancing silica solubility at high *P* conditions becomes clearer.

Comparison with thermodynamic modeling

We compared the measured quartz solubilities in 0.50 and 1.50 *m* Na_2CO_3 with thermodynamically predicted solubilities at similar *P* and *T* conditions based on the equilibration between aqueous silica species, using an equilibrium constant database for aqueous species from the DEW model (Sverjensky et al. 2014; Huang and Sverjensky 2019) and the EQ3NR code (Wolery 1992). In this calculation, we assumed that the oxygen fugacity was near the fayalite–magnetite–quartz (FMQ) buffer, because Schmidt (2014) reported no CH_4 formation in Na_2CO_3 solutions in equilibrium with quartz using an experimental setup similar to ours. We also confirmed that the calculated solubilities were not significantly changed by carbon speciation under more oxidized conditions than that of the FMQ buffer. It should be noted that carbon species were predicted to be mainly electrically neutral under these conditions, which is not consistent with the observed Raman band. In Fig. 2, we showed the thermodynamically predicted silica solubility curves in 0.5 and 1.5 *m* Na_2CO_3 solutions at 1.0 and 1.5 GPa, where the aqueous silica species were $Si(OH)_4$, $Si(OH)_3O^-$, $Si_2O(OH)_6$, and $Si_3O_2(OH)_8$. These curves were lower than our lowest estimation of quartz solubility. Aranovich et al. (2020) also reported that the quartz solubility in Na_2CO_3 solutions based only on the above species underestimated the values at lower pressure ranges (0.4 and 0.5 GPa). Our solubility data, together with those of Aranovich et al. (2020), indicated that the available speciation modeling was insufficient to explain the high quartz solubilities and aqueous speciation in the Na_2CO_3 solution at high *P*–*T* conditions.

High quartz solubility associated with the formation of oligomers

The solubility of silica in aqueous solutions rapidly increases at levels of pH > 9 under ambient conditions (Iler 1979). The studied Na_2CO_3 and NaOH solutions were alkaline, involving the hydrolysis reaction of aqueous carbonate species ($CO_3^{2-} + H_2O = HCO_3^- + OH^-$) or the dissociation of NaOH ($NaOH = Na^+ + OH^-$). The present study showed the favorable formation of HCO_3^- in Na_2CO_3 solutions in the quartz-saturated condition compared to the quartz-undersaturated condition (Fig. 7), which can readily be explained by the consumption of OH^- through the reaction with quartz. Schmidt (2014) demonstrated that the formation of the deprotonated silica monomers in the solutions ($SiO_2(s) + H_2O + OH^- = SiO(OH)_3^-$) reflected the higher quartz solubility in Na_2CO_3 solutions than that in pure H_2O. Our Raman spectroscopic studies confirmed the higher intensities of the monomer bands in the Na_2CO_3 and NaOH solutions than those in pure H_2O (Fig. 5), with the presence of deprotonated monomers up to our highest experimental conditions of 750 °C and 1.5 GPa. Together with the results of Schmidt (2014), we have verified that the formation of deprotonated monomers contributed to the high quartz solubility in the Na_2CO_3 solutions.

Furthermore, the present study newly observed the bridging oxygen band in the Raman spectra of the Na_2CO_3 solutions, which indicates the formation of silica oligomers (Figs. 3, 4, and 5). In particular, the Raman band regions of the tetrahedral symmetric Si–O stretching of structural Q^n units indicate that at least dimeric silicates or chain silicate species, including Q^1 units, are present in the solutions (Fig. 5). To quantify the relative concentrations of species in aqueous solutions and melts, the previous studies considered the ratios of the tetrahedral symmetric stretching band of Q^n species, which are assumed to have the same Raman scattering cross-sectional area (e.g., Mysen 2010; Mysen et al. 2013; Steele-MacInnis and Schmidt 2014). However, the intensities of the detected tetrahedral symmetric stretching bands of Q^1 units in our Na_2CO_3 and NaOH solutions were too low to detect differences in the Q^1/Q^0 ratios between the solutions. Instead, we used the ratio of the intense bridging oxygen Si–O–Si symmetric stretching band to the tetrahedral symmetric stretching band of Q^0 (A_{600}/A_{770}) in a similar manner to Hunt et al. (2011). Comparison of the A_{600}/A_{770} obtained under different *P*–*T* conditions requires the assumption that the ratios of the relative Raman scattering cross-sectional factors are independent of *P* and *T*. Steele-MacInnis and Schmidt (2014) reported no detectable change in the silicate band intensities with increasing *P* at constant *T* and SiO_2 concentrations. Thus, we compared the ratios among spectra of different solutions under similar *T* conditions. Figure 8a shows the integrated intensity ratios, A_{600}/A_{770}, in the quartz-saturated Na_2CO_3, NaOH, and H_2O solutions at *P* = 0.8–1.5 GPa as a function of *T*. The ratios generally increased in the following order: H_2O < 0.47 *m* NaOH < 0.50 *m* Na_2CO_3 < 1.50 *m* Na_2CO_3. In addtion, the increase in the ratios corresponded to the elevation of silica solubility determined by the in-situ observations of the complete dissolution of quartz (Fig. 8b). If the ratios were simply proportional to the concentration ratios of oligomeric species to monomers, the increase in silica oligomers in the solutions would account for the observed high quartz solubilities in the Na_2CO_3 and NaOH solutions. The ratios could also be increased by the formation of silica oligomers with different Raman scattering cross-sectional factors with increasing silica concentration. Therefore, the observed high solubility of quartz in the Na_2CO_3 and NaOH solutions is assumed to have resulted from the formation of silica oligomers in addition to the neutral and deprotonated monomers.

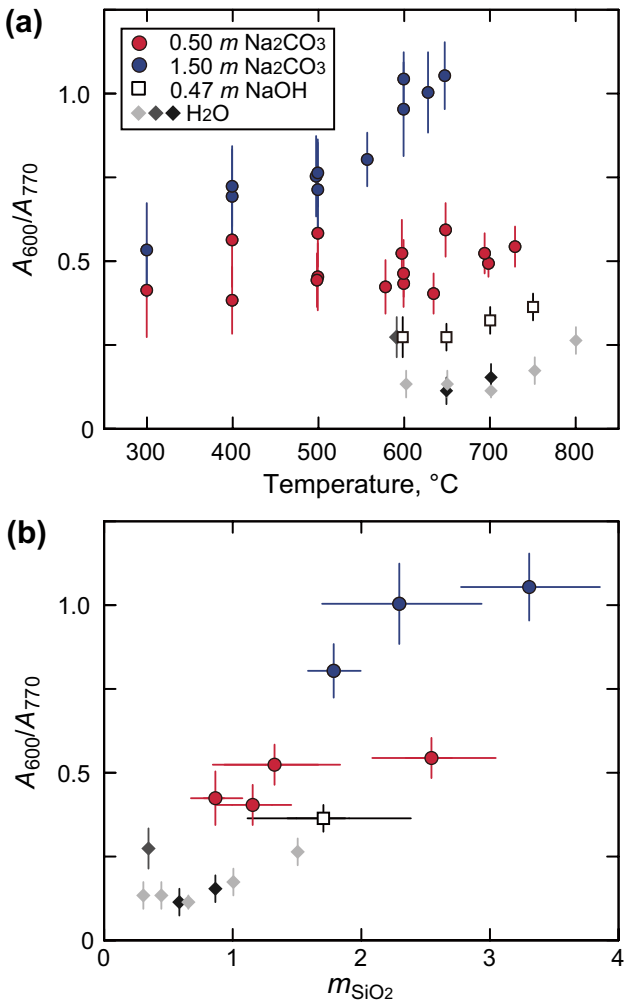

Fig. 8 **a** The integrated intensity ratios of the oligomeric silica species band area to the monomer band area (A_{600}/A_{770}) as a function of temperature (and pressure) and **b** as a function of solubility of quartz determined by in-situ observations. Molal concentrations of silica in H_2O at the experimental *P* and *T* were calculated based on the DEW model (Sverjensky et al. 2014; Huang and Sverjensky 2019)

Silica speciation in alkaline high *P–T* solutions

Based on our solubility data and Raman observations, the oligomeric silica species contribute to the high quartz solubility in alkaline Na_2CO_3 and NaOH solutions under high *P–T* conditions. In particular, the Raman band regions of the tetrahedral symmetric Si–O stretching of structural units Q^n indicate that at least dimeric silicates or chain silicate species, including Q^1 units, are present in the solutions. This suggests that the deprotonated dimer, $Si_2O(OH)_5O^-$, could be present in quartz-saturated alkaline solutions at high *P–T* conditions, as proposed by Aranovich et al. (2020). However, we could not infer the presence of the deprotonated dimers from the Si–O^- stretching Raman band, which appears at ~ 1050 cm^{-1} in the alkaline silicate solutions under ambient conditions and up to 2 GPa (e.g., Hunt et al. 2011). On the other hand, our experiments confirmed the presence of deprotonated monomers in the quartz-saturated Na_2CO_3 and NaOH solutions under all experimental conditions. As the deprotonation of silica dimers and trimers lowers the Gibbs free energy more efficiently than that of the silica monomers in aqueous solutions at room temperature to 450 K (Tossell and Sahai 2000; Mora-Fonz et al. 2007), the deprotonated oligomers could be favorably present in the solutions even at elevated *P–T* conditions. Other possible stable silica oligomers are ion pairs between sodium cations and deprotonated silica oligomers or sodium–silicate complexes, as observed in alkali–silicate solutions under ambient conditions by NMR spectroscopy (Kinrade and Swaddle 1986; McCormick et al. 1989) and fast atom bombardment mass spectroscopy (FAB-MS; Tanaka and Takahashi 1999). Manning et al. (2010) and Wohlers et al. (2011) demonstrated the presence of polymerized Na–Al–Si complexes in aqueous fluids in equilibrium with albite + paragonite + quartz or jadeite + paragonite + quartz at 350–600 °C and 1–2.25 GPa. Although evidence for oligomers involving alkali metals was not directly inferred from the in-situ Raman spectroscopic studies, the effect of alkali metal cations on aqueous silicate equilibria is indicated by the differences in the Raman spectra and integrated intensity ratios between the quartz-saturated 0.50 *m* Na_2CO_3 and 0.47 *m* NaOH solutions. The equilibria involving such oligomers at elevated *P–T* conditions will accurately describe silicate solubility in alkaline fluids.

Implications for element transfer in deep subduction zones

The present study suggests that alkaline fluids can dissolve a significant amount of silica compared to pure H_2O at elevated *P–T* conditions, which is explained by the formation of neutral and deprotonated monomers and the subsequent formation of oligomers. The presence of deprotonated monomers under all experimental conditions suggested the presence of deprotonated and other possible oligomers such as ion pairs between sodium cations and anionic deprotonated silica oligomers. The presence of anionic silica species in alkaline fluids enhances the attractive electrostatic force between opposite ions, which acts as an effective ligand for certain metal ions or complexes. For example, the interaction energies of gold complexes with silica species depend on the pH conditions (Mohammadnejad et al. 2017). Additional examples are Zr and Ti, which are representatives of nominally insoluble high field strength elements. Only SiO_2 components in aqueous fluids did not significantly enhance the solubility of Ti and Zr (Antignano and Manning 2008; Bernini et al. 2013), while the addition of NS2 or NS3 glass or albite components to pure H_2O enhanced the solubility

of Ti and Zr by producing alkaline silicate-rich fluids similar to our experimental system (Antignano and Manning 2008; Manning et al. 2008; Wilke et al. 2012; Louvel et al. 2013). Based on X-ray absorption spectroscopy, Louvel et al. (2013) found that Zr dissolved by forming alkali–zirconosilicate clusters via octahedral coordination with oxygen and Si(Na) second neighbors. The anionic silica species and subsequently formed silica oligomers in alkaline fluids are thus assumed to affect the solubility of these metals by forming complexes.

Conclusions

1. The solubilities of quartz in 0.50 and 1.50 *m* Na_2CO_3 solutions at 558–730 °C and 0.84–1.52 GPa indicated the enhancing effect of Na_2CO_3 on quartz solubility at elevated *P*–*T* conditions. The present study, together with Aranovich et al. (2020), showed that the conventional aqueous silica species [$Si(OH)_4$, $Si(OH)_3O^-$, $Si_2O(OH)_6$, and $Si_3O_2(OH)_8$] alone were insufficient to describe the observed high solubility.
2. The Raman spectra of the quartz-saturated Na_2CO_3 and NaOH solutions exhibited tetrahedral symmetric stretching bands under the experimental conditions. The low frequency and broad FWHM of the bands were interpreted to be due to the deprotonated monomer $Si(OH)_3O^-$ in addition to the neutral monomer $Si(OH)_4$.
3. We newly confirmed the intense bridging oxygen band and the tetrahedral symmetric stretching band of Q^1 units, suggesting the formation of silica oligomers in the solutions. The integrated intensity ratios of the bridging oxygen band area to the monomer band area increased in the following order: $H_2O < 0.47$ *m* NaOH < 0.50 *m* $Na_2CO_3 < 1.50$ *m* Na_2CO_3. The increase in the ratios corresponded to the elevation of quartz solubilities, suggesting that oligomers contributed to the high solubility.
4. Considering the presence of deprotonated monomers under all experimental conditions, we assumed that energetically favorable oligomer deprotonation occurred in the solutions. Sodium–silicate complexes or ion pairs between sodium cations and deprotonated silica oligomers were also possible, although these were not confirmed by in-situ Raman spectroscopic studies. The anionic silica species or oligomers formed in alkaline silicate fluids may act as effective ligands for certain metal ions or complexes in deep subduction zones.

Acknowledgements We are grateful for constructive reviews from two anonymous referees and constructive editorial evaluations from Hans Keppler. We also appreciate Hans Keppler for the advice on the pressure scale for the hydrothermal diamond anvil cell experiments; Hironobu Harada for his support of the titration analysis. In addition, N.T. and T.T. thank Yoshihide Ogasawara for donating a micro-Raman facility to CNEAS.

Author contributions N.T. devised the project, conducted the experiments, analyzed and interpreted the experimental data, and drafted the manuscript. T.T. and M.N. supervised the project, interpreted the experimental data, and contributed to the writing of the manuscript. S.K. provided basic DAC methods and aided in conducting preliminary experiments. All authors read and approved the final manuscript.

Funding This research was supported by the Graduate School of Science and Center for Northeast Asian Studies, Tohoku University, in part by grants from the MEXT/JSPS KAKENHI JP19J21319 to N. Takahashi, JP18H01299 and JP21H01174 to T. Tsujimori, JSPS Japanese–German Graduate Externship, and the International Joint Graduate Program in Earth and Environmental Sciences (GP-EES) of Tohoku University.

Availability of data and materials The dataset analyzed during this study is available from the corresponding author upon reasonable request.

Declarations

Conflict of interest The authors declare that they have no known conflicts or competing interests that could have influenced the work reported in this paper.

References

Anderson GM, Burnham CW (1965) The solubility of quartz in super-critical water. Am J Sci 263:494–511. https://doi.org/10.2475/ajs.263.6.494

Anderson GM, Burnham CW (1967) Reactions of quartz and corundum with aqueous chloride and hydroxide solutions at high temperatures and pressures. Am J Sci 265:12–27. https://doi.org/10.2475/ajs.265.1.12

Anderson AJ, Meredith PR, Bassett WA, Mayanovic RA, Benmore C (2010) The design and application of a new Bassett-type diamond anvil cell for spectroscopic analysis of supercritical aqueous solutions. In: Proceedings of the CNS 2nd Canada–China joint workshop on super critical water-cooled reactors (SCWR)

Antignano A, Manning CE (2008) Rutile solubility in H_2O, H_2O–SiO_2, and H_2O–$NaAlSi_3O_8$ fluids at 0.7–2.0 GPa and 700–1000 °C: implications for mobility of nominally insoluble elements. Chem Geol 255:283–293. https://doi.org/10.1016/j.chemgeo.2008.07.001

Aranovich L, Akinfiev NN, Golunova M (2020) Quartz solubility in sodium carbonate solutions at high pressure and temperature. Chem Geol. https://doi.org/10.1016/j.chemgeo.2020.119699

Arganda-Carreras I, Kaynig V, Rueden C et al (2017) Trainable Weka Segmentation: a machine learning tool for microscopy pixel classification. Bioinformatics 33:2424–2426. https://doi.org/10.1093/bioinformatics/btx180

Audet P, Bürgmann R (2014) Possible control of subduction zone slow-earthquake periodicity by silica enrichment. Nature 510:389–392. https://doi.org/10.1038/nature13391

Audétat A, Keppler H (2005) Solubility of rutile in subduction zone fluids, as determined by experiments in the hydrothermal diamond anvil cell. Earth Planet Sci Lett 232:393–402. https://doi.org/10.1016/j.epsl.2005.01.028

Bebout GE, Barton MD (1989) Fluid flow and metasomatism in a subduction zone hydrothermal system: Catalina Schist terrane, California. Geology 17:976–980. https://doi.org/10.1130/0091-7613(1989)017%3c0976:FFAMIA%3e2.3.CO;2

Bergna HE, Roberts WO (2005) Colloidal silica: fundamentals and applications. CRC Press, Boca Raton

Bernini D, Audétat A, Dolejš D, Keppler H (2013) Zircon solubility in aqueous fluids at high temperatures and pressures. Geochim Cosmochim Acta 119:178–187. https://doi.org/10.1016/j.gca.2013.05.018

Breeding CM, Ague JJ (2002) Slab-derived fluids and quartz-vein formation in an accretionary prism, Otago Schist, New Zealand. Geology 30:499–502. https://doi.org/10.1130/0091-7613(2002)030%3c0499:SDFAQV%3e2.0.CO;2

Brooker MH, Nielsen OF, Praestgaard E (1988) Assessment of correction procedures for reduction of Raman spectra. J Raman Spectrosc 19:71–78. https://doi.org/10.1002/jrs.1250190202

Connolly JAD, Galvez ME (2018) Electrolytic fluid speciation by Gibbs energy minimization and implications for subduction zone mass transfer. Earth Planet Sci Lett 501:90–102. https://doi.org/10.1016/j.epsl.2018.08.024

Dutta PK, Shieh DC (1985) Raman spectral study of the composition of basic silicate solutions. Appl Spectrosc 39:343–346. https://doi.org/10.1366/0003702854248971

Frantz JD (1998) Raman spectra of potassium carbonate and bicarbonate aqueous fluids at elevated temperatures and pressures: comparison with theoretical simulations. Chem Geol 152:211–225. https://doi.org/10.1016/S0009-2541(98)00058-8

Friedman II (1948) The solubility of quartz in sodium carbonate solutions at high temperature. J Am Chem Soc 70:2649–2650. https://doi.org/10.1021/ja01188a010

Galvez ME, Manning CE, Connolly JAD, Rumble D (2015) The solubility of rocks in metamorphic fluids: a model for rock-dominated conditions to upper mantle pressure and temperature. Earth Planet Sci Lett 430:486–498. https://doi.org/10.1016/j.epsl.2015.06.019

Galvez ME, Connolly JAD, Manning CE (2016) Implications for metal and volatile cycles from the pH of subduction zone fluids. Nature 539:420–424. https://doi.org/10.1038/nature20103

Gout R, Pokrovski GS, Schott J, Zwick A (2000) Raman spectroscopic study of aluminum silicate complexes at 20 °C in basic solutions. J Solut Chem 29:1173–1186. https://doi.org/10.1023/A:1026428027101

Huang F, Sverjensky DA (2019) Extended Deep Earth Water Model for predicting major element mantle metasomatism. Geochim Cosmochim Acta 254:192–230. https://doi.org/10.1016/j.gca.2019.03.027

Hunt JD, Kavner A, Schauble EA, Snyder D, Manning CE (2011) Polymerization of aqueous silica in H_2O–K_2O solutions at 25–200 °C and 1 bar to 20 kbar. Chem Geol 283:161–170. https://doi.org/10.1016/j.chemgeo.2010.12.022

Hyndman RD, McCrory PA, Wech A, Kao H, Ague JJ (2015) Cascadia subducting plate fluids channelled to fore-arc mantle corner: ETS and silica deposition. J Geophys Res Solid Earth 120:4344–4358. https://doi.org/10.1002/2015JB011920

Iler RK (1979) The chemistry of silica: solubility, polymerization, colloid and surface properties, and biochemistry of silica. Wiley-Interscience, New York

Kinrade SD, Swaddle TW (1986) Mechanisms of longitudinal ^{29}Si nuclear magnetic relaxation in aqueous alkali-metal silicate solutions. J Am Chem Soc 108:7159–7162. https://doi.org/10.1021/ja00283a004

Kubicki JD, Sykes D (1993) Molecular orbital calculations on $H_6Si_2O_7$ with a variable Si–O–Si angle: implications for the high-pressure vibrational spectra of silicate glasses. Am Mineral 78:253–259

Laliberté M (2009) A model for calculating the heat capacity of aqueous solutions, with updated density and viscosity data. J Chem Eng Data 54:1725–1760. https://doi.org/10.1021/je8008123

Lasaga AC, Gibbs GV (1988) Quantum mechanical potential surfaces and calculations on minerals and molecular clusters. Phys Chem Miner 16:29–41. https://doi.org/10.1007/BF00201327

Louvel M, Sanchez-Valle C, Malfait WJ, Testemale D, Hazemann J-L (2013) Zr complexation in high pressure fluids and silicate melts and implications for the mobilization of HFSE in subduction zones. Geochim Cosmochim Acta 104:281–299. https://doi.org/10.1016/j.gca.2012.11.001

Manning CE (1994) The solubility of quartz in H_2O in the lower crust and upper mantle. Geochim Cosmochim Acta 58:4831–4839. https://doi.org/10.1016/0016-7037(94)90214-3

Manning CE, Wilke M, Schmidt C, Cauzid J (2008) Rutile solubility in albite–H_2O and $Na_2Si_3O_7$–H_2O at high temperatures and pressures by in-situ synchrotron radiation micro-XRF. Earth Planet Sci Lett 272:730–737. https://doi.org/10.1016/j.epsl.2008.06.004

Manning CE, Antignano A, Lin HA (2010) Premelting polymerization of crustal and mantle fluids, as indicated by the solubility of albite + paragonite + quartz in H2O at 1 GPa and 350–620 °C. Earth Planet Sci Lett 292:325–336. https://doi.org/10.1016/j.epsl.2010.01.044

McCormick AV, Bell AT, Radke CJ (1989) Evidence from alkali-metal NMR spectroscopy for ion pairing in alkaline silicate solutions. J Phys Chem 93:1733–1737. https://doi.org/10.1021/j100342a013

Mohammadnejad S, Provis JL, van Deventer JSJ (2017) Computational modelling of interactions between gold complexes and silicates. Comput Theor Chem 1101:113–121. https://doi.org/10.1016/j.comptc.2016.12.036

Mora-Fonz MJ, Catlow CRA, Lewis DW (2007) Modeling aqueous silica chemistry in alkali media. J Phys Chem C 111:18155–18158. https://doi.org/10.1021/jp077153u

Mysen BO (2010) Speciation and mixing behavior of silica-saturated aqueous fluid at high temperature and pressure. Am Mineral 95:1807–1816. https://doi.org/10.2138/am.2010.3539

Mysen BO (2018) Silicate solution, cation properties, and mass transfer by aqueous fluid in the Earth's interior. Prog Earth Planet Sci 5:40. https://doi.org/10.1186/s40645-018-0198-1

Mysen BO, Mibe K, Chou I-M, Bassett WA (2013) Structure and equilibria among silicate species in aqueous fluids in the upper mantle: experimental SiO_2-H_2O and MgO-SiO_2-H_2O data recorded in situ to 900 °C and 5.4 GPa. J Geophys Res Solid Earth 118:6076–6085. https://doi.org/10.1002/2013JB010537

Newton RC, Manning CE (2000) Quartz solubility in H_2O-NaCl and H_2O-CO_2 solutions at deep crust-upper mantle pressures and temperatures: 2–15 kbar and 500–900 °C. Geochim Cosmochim Acta 64:2993–3005. https://doi.org/10.1016/S0016-7037(00)00402-6

Newton RC, Manning CE (2002) Solubility of enstatite + forsterite in H2O at deep crust/upper mantle conditions: 4 to 15 kbar and 700 to 900 °C. Geochim Cosmochim Acta 66:4165–4176. https://doi.org/10.1016/S0016-7037(02)00998-5

Newton RC, Manning CE (2008) Thermodynamics of SiO_2–H_2O fluid near the upper critical end point from quartz solubility

measurements at 10 kbar. Earth Planet Sci Lett 274:241–249. https://doi.org/10.1016/j.epsl.2008.07.028

Rudolph WW, Irmer G, Königsberger E (2008) Speciation studies in aqueous HCO_3^-–CO_3^{2-} solutions. A combined Raman spectroscopic and thermodynamic study. Dalton Trans 7:900–908. https://doi.org/10.1039/B713254A

Schindelin J, Arganda-Carreras I, Frise E et al (2012) Fiji: an open-source platform for biological-image analysis. Nat Methods 9:676–682. https://doi.org/10.1038/nmeth.2019

Schmidt C (2009) Raman spectroscopic study of a $H_2O + Na_2SO_4$ solution at 21–600 °C and 0.1 MPa to 1.1 GPa: relative differential ν_1-SO_4^{2-} Raman scattering cross sections and evidence of the liquid–liquid transition. Geochim Cosmochim Acta 73:425–437. https://doi.org/10.1016/j.gca.2008.10.019

Schmidt C (2014) Raman spectroscopic determination of carbon speciation and quartz solubility in $H_2O + Na_2CO_3$ and $H_2O + NaHCO_3$ fluids to 600 °C and 1.53 GPa. Geochim Cosmochim Acta 145:281–296. https://doi.org/10.1016/j.gca.2014.09.009

Schmidt C, Ziemann MA (2000) In-situ Raman spectroscopy of quartz: a pressure sensor for hydrothermal diamond-anvil cell experiments at elevated temperatures. Am Mineral 85:1725–1734. https://doi.org/10.2138/am-2000-11-1216

Schmidt C, Steele-MacInnis M, Watenphul A, Wilke M (2013) Calibration of zircon as a Raman spectroscopic pressure sensor to high temperatures and application to water–silicate melt systems. Am Mineral 98:643–650. https://doi.org/10.2138/am.2013.4143

Shmulovich KI, Graham CM, Yardley BWD (2001) Quartz, albite and diopside solubilities in H_2O–NaCl and H_2O–CO_2 fluids at 0.5–0.9 GPa. Contrib Mineral Petrol 141:95–108. https://doi.org/10.1007/s004100000224

Shmulovich KI, Yardley BWD, Graham CM (2006) Solubility of quartz in crustal fluids: experiments and general equations for salt solutions and H_2O–CO_2 mixtures at 400–800 °C and 0.1–0.9 GPa. Geofluids 6:154–167. https://doi.org/10.1111/j.1468-8123.2006.00140.x

Spiekermann G, Steele-MacInnis M, Kowalski PM, Schmidt C, Jahn S (2012a) Vibrational mode frequencies of H_4SiO_4, D_4SiO_4, $H_6Si_2O_7$, and $H_6Si_3O_9$ in aqueous environment, obtained from *ab initio* molecular dynamics. J Chem Phys 137:164506. https://doi.org/10.1063/1.4761824

Spiekermann G, Steele-MacInnis M, Schmidt C, Jahn S (2012b) Vibrational mode frequencies of silica species in SiO_2-H_2O liquids and glasses from *ab initio* molecular dynamics. J Chem Phys 136:154501. https://doi.org/10.1063/1.3703667

Steele-MacInnis M, Schmidt C (2014) Silicate speciation in H_2O–Na_2O–SiO_2 fluids from 3 to 40 mol% SiO_2, to 600 °C and 2 GPa. Geochim Cosmochim Acta 136:126–141. https://doi.org/10.1016/j.gca.2014.04.009

Sverjensky DA, Harrison B, Azzolini D (2014) Water in the deep Earth: the dielectric constant and the solubilities of quartz and corundum to 60 kb and 1200 °C. Geochim Cosmochim Acta 129:125–145. https://doi.org/10.1016/j.gca.2013.12.019

Tanaka M, Takahashi K (1999) The identification of chemical species of silica in sodium hydroxide, potassium hydroxide and sodium chloride solutions by FAB-MS. Anal Sci 15:1241–1250. https://doi.org/10.2116/analsci.15.1241

Tossell JA, Sahai N (2000) Calculating the acidity of silanols and related oxyacids in aqueous solution. Geochim Cosmochim Acta 64:4097–4113. https://doi.org/10.1016/S0016-7037(00)00497-X

Wagner W, Pruβ A (2002) The IAPWS formulation 1995 for the thermodynamic properties of ordinary water substance for general and scientific use. J Phys Chem Ref Data 31:387–535. https://doi.org/10.1063/1.1461829

Wilke M, Schmidt C, Dubrail J et al (2012) Zircon solubility and zirconium complexation in $H_2O + Na_2O + SiO_2 \pm Al_2O_3$ fluids at high pressure and temperature. Earth Planet Sci Lett 349–350:15–25. https://doi.org/10.1016/j.epsl.2012.06.054

Wohlers A, Manning CE, Thompson AB (2011) Experimental investigation of the solubility of albite and jadeite in H_2O, with paragonite+quartz at 500 and 600 °C, and 1–2.25 GPa. Geochim Cosmochim Acta 75:2924–2939. https://doi.org/10.1016/j.gca.2011.02.028

Wolery TJ (1992) EQ3NR, A computer program for geochemical aqueous speciation-solubility calculations: Theoretical manual, user's guide, and related documenta-tion (Version 7.0). Lawrence Livermore Natl. Lab. UCRL-MA-110662, pt III

Yardley BWD, Bottrell SH (1992) Silica mobility and fluid movement during metamorphism of the Connemara schists, Ireland. J Metamorph Geol 10:453–464. https://doi.org/10.1111/j.1525-1314.1992.tb00096.x

Zhang Z, Duan Z (2005) Prediction of the *PVT* properties of water over wide range of temperatures and pressures from molecular dynamics simulation. Phys Earth Planet Inter 149:335–354. https://doi.org/10.1016/j.pepi.2004.11.003

Zotov N, Keppler H (2000) In-situ Raman spectra of dissolved silica species in aqueous fluids to 900 °C and 14 kbar. Am Mineral 85:600–604. https://doi.org/10.2138/am-2000-0423

Zotov N, Keppler H (2002) Silica speciation in aqueous fluids at high pressures and high temperatures. Chem Geol 184:71–82. https://doi.org/10.1016/S0009-2541(01)00353-9